

Nanoscale

Accepted Manuscript



This is an *Accepted Manuscript*, which has been through the Royal Society of Chemistry peer review process and has been accepted for publication.

Accepted Manuscripts are published online shortly after acceptance, before technical editing, formatting and proof reading. Using this free service, authors can make their results available to the community, in citable form, before we publish the edited article. We will replace this *Accepted Manuscript* with the edited and formatted *Advance Article* as soon as it is available.

You can find more information about *Accepted Manuscripts* in the [Information for Authors](#).

Please note that technical editing may introduce minor changes to the text and/or graphics, which may alter content. The journal's standard [Terms & Conditions](#) and the [Ethical guidelines](#) still apply. In no event shall the Royal Society of Chemistry be held responsible for any errors or omissions in this *Accepted Manuscript* or any consequences arising from the use of any information it contains.

Anisotropic mechanoresponse of energetic crystallites: a quantum molecular dynamics study of nano-collision

Ying Li,^{a,b} Rajiv K. Kalia,^b Masaaki Misawa,^{b,c} Aiichiro Nakano,^b Ken-ichi Nomura,^b Kohei Shimamura,^{b,c,d} Fuyuki Shimojo,^c and Priya Vashishta^b

^a Argonne Leadership Computing Facility, Argonne National Laboratory, Argonne, Illinois 60439, USA, E-mail: yingli@anl.gov; Tel: +1-630-252-3394

^b Collaboratory for Advanced Computing and Simulations, Department of Physics and Astronomy, Department of Computer Science, Department of Chemical Engineering and Material Science, University of Southern California, Los Angeles, California 90089-0242, USA.

^c Department of Physics, Kumamoto University, Kumamoto 860-8555, Japan

^d Graduate School of System Informatics, Kobe University, Kobe 657-8501, Japan

† Electronic Supplementary Information (ESI) available. See DOI: 10.1039/x0xx00000x

At the nanoscale, chemistry can happen quite differently due to mechanical forces selectively break chemical bonds of materials. The interaction between chemistry and mechanical forces can be classified as mechanochemistry. An archetypal mechanochemistry occurs at the nanoscale in anisotropic detonating of a board class of layered energetic molecular crystals bonded by inter-layer van der Waals (vdW) interactions. Here, we introduce an *ab initio* study of the collision, in which quantum molecular dynamic simulations of binary collision between energetic vdW crystallites, TATB molecules, reveal atomistic mechanisms of anisotropic shock sensitivity. The highly sensitive lateral collision was found to originate from the twisting and bending to breaking of nitro-groups mediated by strong intra-layer hydrogen bonds. This causes the closing of the electronic energy gap due to an inverse Jahn-Teller effect. On the other hand, insensitive collision normal to multilayers is accomplished by more delocalized molecular deformations mediated by inter-layer interactions. Our nano collision studies provide much needed atomistic understanding toward rational design of insensitive energetic nanomaterials and detonation synthesis of novel nanomaterials.

Introduction

Rational design of materials is possible due to advancements in recent experimental techniques, in which chemical reactions are controlled mechanically.¹⁻⁴ In so-called mechanochemistry, mechanical forces selectively break covalent bonds. Such

mechanochemistry can now be studied at the nanoscale with recently developed theoretical nanoreactors⁵ and nanoscale impact experiments.⁶ An illustration is the application of sonication of polymers, where polymers exhibit different reaction pathways when exposing under ultrasound other than light or heat.⁷ Another prime example is the detonation of energetic materials, where mechanical shock waves initiate exothermic reactions to self-sustain wave propagation.^{8,9} In typical energetic molecular crystals, it takes only 10^{-13} s (*i.e.*, the period of one molecular vibration) for a detonation wave front to pass through each molecule. This timescale is too short for chemical reactions to be thermally activated. Consequently, reactions are likely initiated athermally via mechanical activation.¹⁰ An archetypal mechanochemistry appears during detonation of triaminotrinitrobenzene (TATB) or 2,4,6-triamino-1,3,5-trinitrobenzene. It was suggested theoretically that mechanical bending of a nitrate group in a TATB molecule closes the energy gap between the highest occupied molecular orbital (HOMO) and the lowest unoccupied molecular orbital (LUMO) through an inverse Jahn-Teller effect.^{10,11} The closing of the HOMO-LUMO gap liberates bonding electrons to initiate chemical reactions.

TATB fits into the category of layered energetic molecular crystals, which is extremely insensitive to shock or impact. Due to the hinder of detonating by accident, TATB acquires favours for applications in safety engineering.¹² The inter-layer van der Waals (vdW) interactions¹³⁻¹⁶ hold the layered crystal structure of TATB molecules, which is similar to vdW materials that are gaining growing attention due to their unique physical and chemical properties.^{17,18} Within each layer, on the other hand, these energetic crystals are inter-bonded by a strong hydrogen-bond network in addition to intra-molecular covalent bonds. The interplay between inter-layer vdW forces and intra-layer hydrogen bonds is expected to dictate anisotropic detonation behaviours of these energetic vdW crystals. A fundamental scientific question is: How does the interplay of vdW forces and hydrogen bonds determine anisotropic mechanochemistry in energetic vdW crystals? Recent nanoscale impact experiments have studied mechanical responses of multilayer vdW materials,⁶ and similar mechanochemical anisotropy was studied previously using binary collision of pentaerythritol tetranitrate (PETN) molecules.^{19,20} However, such bi-molecular collision cannot capture the inter-layer/intra-layer effects of interests. To address this key issue, we here introduce an *ab initio* study of collision, in which the collision of TATB crystallites is studied using quantum molecular dynamics (QMD) simulations.²¹⁻²⁴ QMD follows the trajectories of all atoms while computing interatomic interactions quantum mechanically

based on density functional theory (DFT).²⁵ Our nanocollider augments recently developed nanoreactor⁵ and nanoscale impact⁶ technologies, thereby providing not only interpretation of experimental findings but also the discovery of new reaction pathways.

Simulation methods

TATB is a rather intensive aromatic explosive, based on the basic six-carbon benzene ring structure with three nitro functional groups (NO₂) and three amine (NH₂) groups attached,

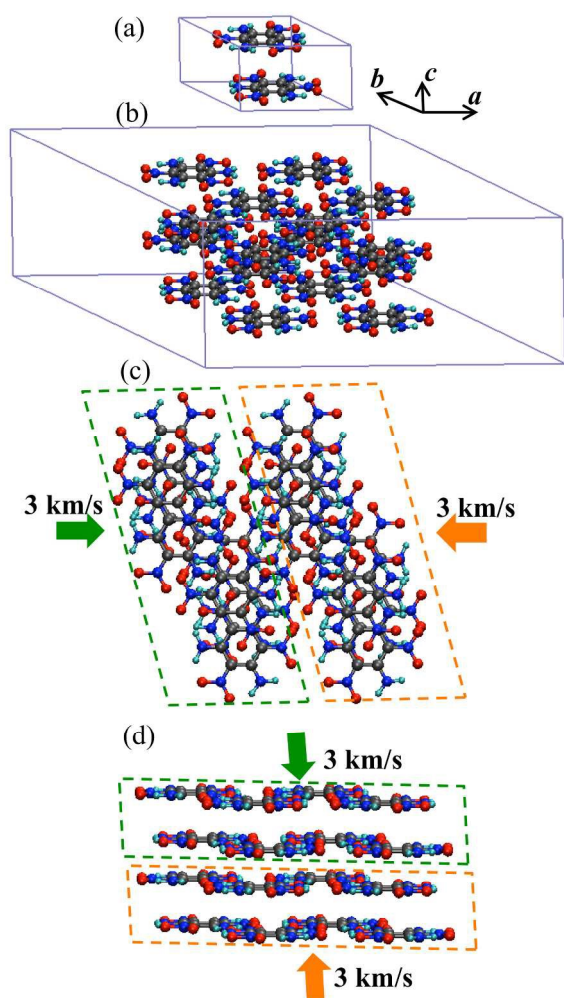


Fig. 1 Simulated TATB nanocrystallites. (a) TATB molecular crystal unit cell structure (b) Simulation box containing 16 TATB molecules. (c) Schematic of the *a*-axis collision, where two crystallites enclosed respectively by green and orange dashed lines collide with speed of 3 km/s indicated by the arrows. (d) The same as (c) for the *c*-axis collision.

alternating around the ring.²⁶⁻²⁸

There are two TATB molecules in each triclinic unit cell²⁹ with lattice parameters $a = 9.01 \text{ \AA}$, $b = 9.028 \text{ \AA}$, $c = 6.812 \text{ \AA}$, $\alpha = 108.58^\circ$, $\beta = 91.82^\circ$, and $\gamma = 119.97^\circ$ (Fig. 1(a)). The initial simulation box consists of a TATB crystalline unit cells repeated $2 \times 2 \times 2$ times in the *a*, *b* and *c* crystallographic directions with 20 \AA extra space added along each direction (Fig. 1(b)). To study crystalline anisotropy in TATB, we perform two sets of simulations, each use different random seeds for initiating velocity for atoms and wave functions for electrons: By assigning opposing initial velocities of 3 km/s to two crystallites, each containing 8 molecules, the crystallites collide along the *a*-axis (Fig. 1(c)) and *c*-axis (Fig. 1(d)) directions, respectively. This amounts to a collision speed of 6

km/s, which is approximate below the detonation speed of TATB crystals.³⁰ In total, we have six different systems set up for 6 km/s *a*-axis and *c*-axis collisions.

In our QMD simulations, electronic states are calculated using the projector-augmented-wave (PAW) method.³¹ The generalized gradient approximation (GGA),³² along with vdW correction,³³ is used for the exchange-correlation energy with non-linear core corrections based on the DFT-D method.³⁴ The momentum-space formalism is utilized, where the plane-wave cutoff energies are 30 and 250 Ry for electronic pseudo-wave functions and pseudo-charge density, respectively, and the gamma point is used in the Brillouin zone. The energy functional is minimized iteratively using a preconditioned conjugated gradient method. Projector functions are generated for the 2s and 2p states of C, N and O, and the 1s state for H. Our QMD code has been implemented on parallel computers by a hybrid approach combining spatial decomposition (*i.e.*, distributing real-space or reciprocal-space grid points among processors) and band decomposition (*i.e.*, assigning the calculations of different Kohn-Sham orbitals to different processors).^{24,35} Quasi-Newton method is used for structural optimization prior to QMD simulations. QMD simulations are carried out using interatomic forces that are computed quantum mechanically based on the Hellmann-Feynman theorem. The equations of motion are integrated numerically with a time step of 10 a.u. (~ 0.24 fs).

Results

To study chemical reaction pathways, we perform fragment analysis, where a cluster of covalently bonded atoms is counted as a fragment. Here a pair of atoms is considered connected if their distance is shorter than a critical value, but is slightly longer than the corresponding covalent bond length. Figures 2(a) and 2(b) show the number of fragments are a function of time for the *a*-axis and *c*-axis collisions, respectively. In the case of *a*-axis collision, Fig. 2(a) shows the number of fragments with a reasonable statistical discrepancy, but overall consistency for different trajectories, for example, a number of NO₂ fragments are produced as shown in Fig. 2(a). In contrast, Fig. 2(b) shows no bond breakage for the *c*-axis collision. These results indicate that the *a*-axis collision is more sensitive compared with the *c*-axis collision. Production of NO₂ as the initial reaction product is consistent with the case of bi-molecular collision in PETN¹⁹ and shock-induced detonation of cyclotrimethylenetrinitramine (RDX) crystal.³⁶⁻³⁸

The anisotropic sensitivity shown above is also reflected in the temperature of the system. To compute the temperature, we take account of the average kinetic energy of the atoms in each individual fragment by subtracting the center-of-mass velocity of the fragment from the velocity of each atom for every trajectory (The concept of temperature is different from the thermal average of the kinetic energy of a solid-state system, because the time scale is too short for chemical reactions to be thermally activated). Figures 2(c) and 2(d) show the temperatures of the six systems as a function of time. For the *a*-axis collision, the temperature generally rises rapidly and reaches 1,350 K by the end of the simulation (Fig. 2(c)). On the hand, for the *c*-axis collision, the temperature generally exhibits a periodic oscillation reflecting multiple collisions among TATB layers (Fig. 2(d)). The temperature for the *c*-axis collision remains around 1,000 K, which is much lower than that in the *a*-axis collision. The more rapid temperature rise in the *a*-axis collision indicates that the kinetic energy of the colliding crystallites is converted to molecular vibrational modes more effectively compared to the *c*-axis collision.³⁹ The different temperatures between Figs. 2(c) and 2(d) arise from very different intermediate chemical reactions between the *a*-axis and *c*-axis collisions within 100 fs, illustrated, *e.g.*, by different intermediate products shown in Figs. 2(a) and 2(b). Consequently, different amounts of energy are released, thereby resulting in different temperatures. This is a manifestation of the mechanochemical initiation of chemical reactions, which are highly sensitive to molecular shapes and crystallographic packing. As all systems complete reactions to produce the same final products, however, they should reach the same thermodynamic state. According to previous simulations on TATB²⁷ and related energetic molecular crystals,³⁸ this is expected to take longer than ns.

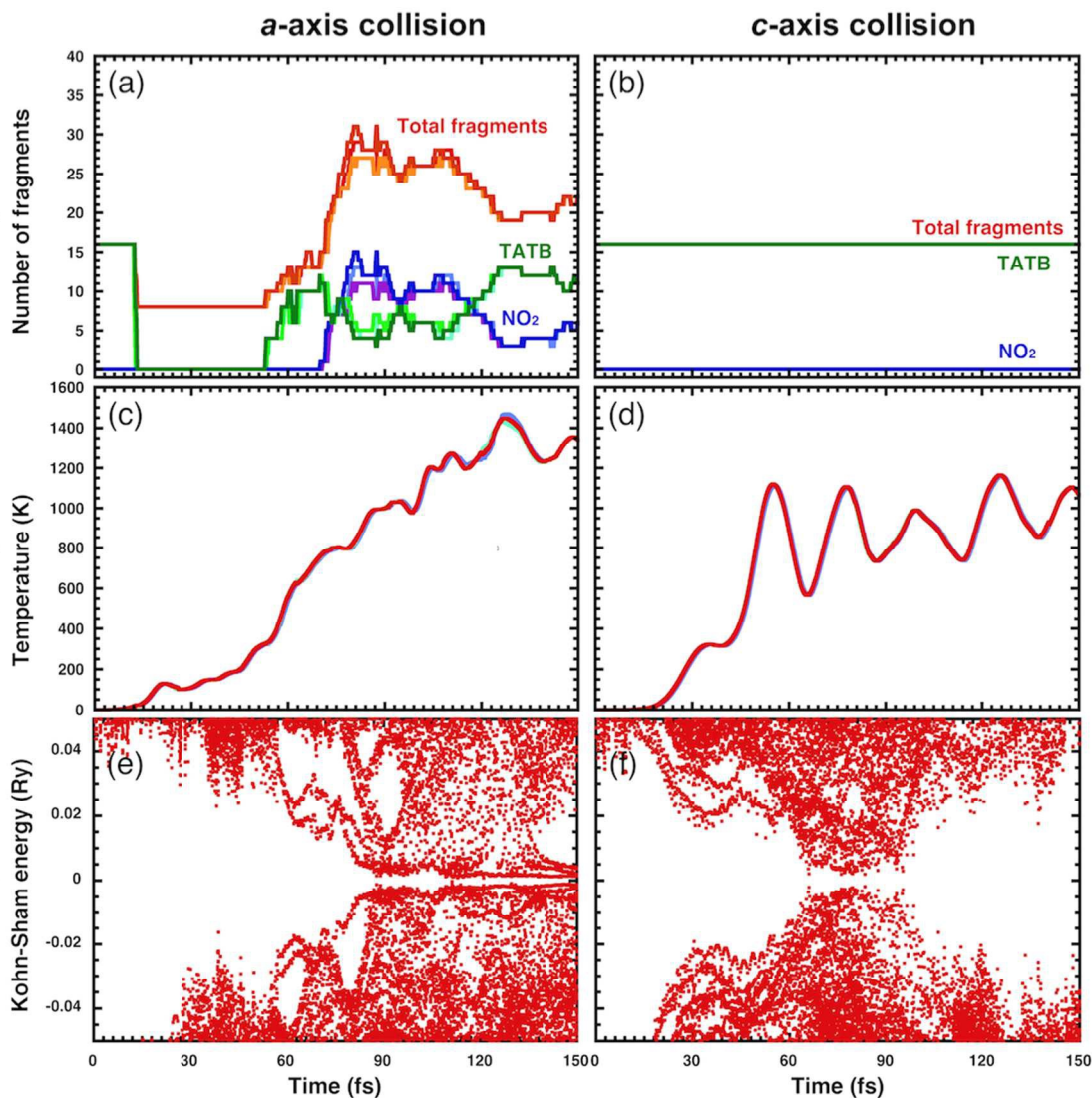


Fig. 2 Time evolution of the a - and c -axis collision simulations. (a) and (b) show the number of molecular fragments, (c) and (d) show the temperature, and (e) and (f) show the Kohn-Sham eigenenergies. The left and right columns are for the a -axis and c -axis collisions, respectively, each with three different trajectories. Also see Fig. S1 for details of Kohn-Sham eigenenergies for the additional trajectories.

Figures 2(e) and 2(f) plot the electronic Kohn-Sham eigenenergies as a function of time for one of the a -axis and c -axis collisions, respectively (other four more trajectories also show the similar look of the Kohn-Sham eigenenergies as a function of time for 6 km/s a - and c -axis collisions, see also Fig. S1(a), S1(b), S1(c) and S1(d), in Electronic Supplementary Information, for details). In Fig. 2(e) for the a -axis collision, the HOMO-LUMO energy gap closes at around 80 fs and remains closed for the entire simulation. In the c -axis collision, the HOMO-LUMO gap also closes at around 80 fs. However, the gap reopens as the two crystallites bounce back after the c -axis collision (Fig. 2(f)) in a sharp contrast to the a -axis collision where the gap remains closed (Fig. 2(e)). Energy-gap closure similar to Figs. 2(e)

and 2(f) were observed in DFT calculation of a single TATB molecule by Manaa.¹¹ His

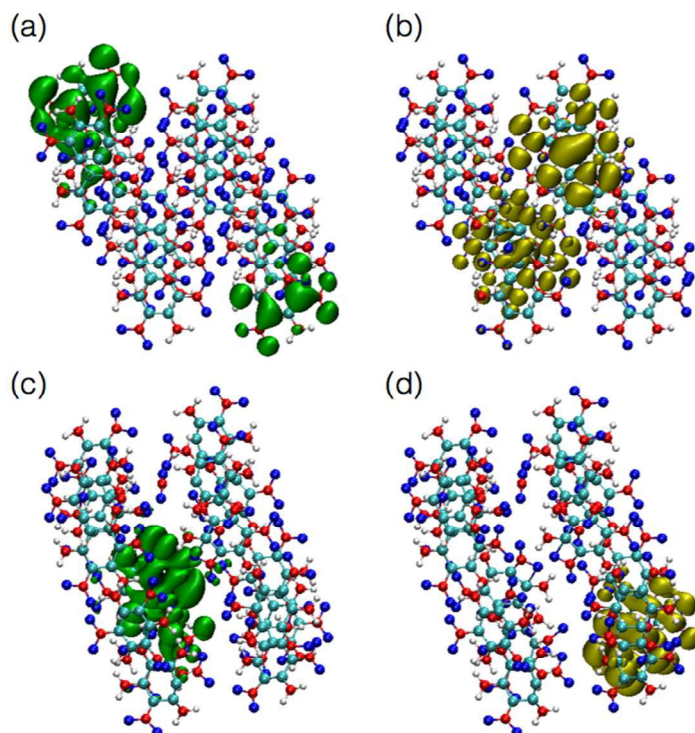


Fig. 3 HOMO and LUMO electron densities during the a -axis collision before and after the band gap closure. Isosurfaces are shown for (a) HOMO before gap closure, (b) LUMO before gap closure, (c) HOMO after gap closure, and (d) LUMO after gap closure.

calculation identifies the closure of the energy gap due to the bending of the nitro-group. As shown below, the gap closure in our simulation is accompanied by twisting and bending of nitro-groups, which is consistent with the results by Manaa.¹¹ The energy degeneracy caused by molecular distortion can be viewed as an inverse Jahn-Teller effect. Here geometrical distortion from the ground state causes the destabilization of the electronic structures (*i.e.*, a closing of the HOMO-LUMO

gap), which in turn causes the liberation of frontier orbitals to promote chemical reactions.^{10, 11} Figure 3 shows the electronic charge densities of the highest occupied molecular orbital (HOMO) and lowest unoccupied molecular orbital (LUMO) before (0 fs) and after (150 fs) the band gap closure during the a -axis collision.

To contrast different reaction mechanisms between the a - and c -axis collisions, the snapshots in Fig. 4 show part of the two simulation systems (see also movies, S1.mov and S2.mov, in Electronic Supplementary Information). Figures 4(a)-4(f) for the a -axis collision shows the production of NO_2 from a TATB molecule. At 10 fs, strong inter-molecular hydrogen bonds are formed between two adjacent TATB molecules (Fig. 4(b)). At 30 fs, the carbon ring in one of the TATB molecules (on the right in Fig. 4(c)) deforms severely due to the contact with another TATB molecule (on the left in Fig. 4(c)). As the carbon ring restores its shape, the inter-molecular hydrogen bonds cause twisting and bending of the NO_2 group

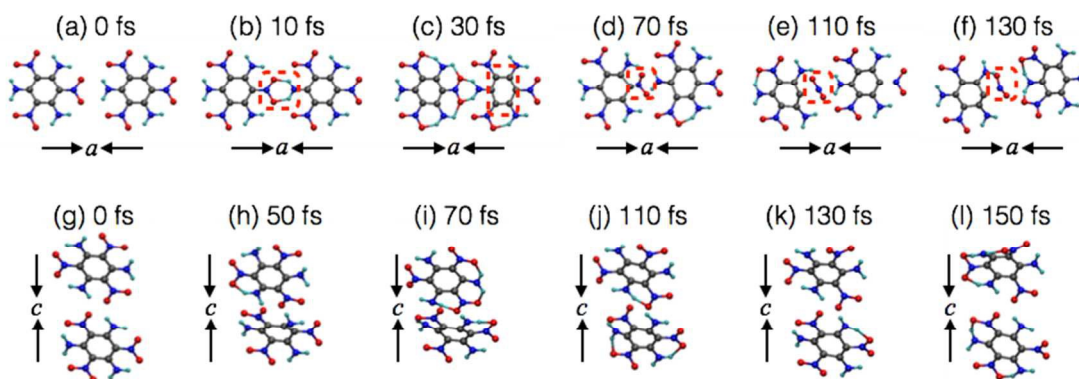


Fig. 4 Atomistics of anisotropic collisions. Snapshots of the a -axis ((a)-(f)) and c -axis ((g)-(l)) collision simulations. Cyan, gray, blue and red spheres represent H, C, N and O atoms, respectively.

at the collision front in the left TATB molecule (Figs. 4(d) and 4(e)). Thus causes the scission of the C-N bond, and the dissociation of an NO_2 molecule (Figs. 4(e) and 4(f)). On the contrary, no reaction is observed in Figures 4(g)-4(l) for the c -axis collision. As TATB molecules approach each other in c -axis collision, hydrogen bonds are formed only within individual TATB molecules in contrast to the formation of inter-molecular hydrogen bonds during the a -axis collision. The marked difference can be understood as following. In the a -axis collision, the two inter-molecular hydrogen bonds push and twist one of the NO_2 groups in the left TATB molecule (Figs. 4(b) and 4(c)). Here, only one C-N bond connecting the NO_2 group to the carbon. On the contrary, in the c -axis collision, the mechanical load is shared by more delocalized deformation of the entire molecule, which is not sufficient to break any covalent bond.

To quantify the NO_2 dissociation in the a -axis collision, we perform a bond overlap population (BOP) analysis⁴⁰ by expanding the electronic wave functions with an atomic-orbital basis set.⁴¹ Based on the formulation generalized to the PAW method,²¹⁻²³ we obtain the gross population Z_i for the i^{th} atom and the BOP O_{ij} for the pair of i^{th} and j^{th} atoms. From Z_i , we estimate the atomic charge, and O_{ij} gives a semi-quantitative estimate of the strength of covalent bonding. As the atomic basis orbitals, we use numerical eigenfunctions of atoms, which are obtained for a chosen atomic energy so that the first node coincides with the desired cutoff radius.⁴² To increase the efficiency of the expansion, the numerical basis orbitals are augmented with the split-valence method.⁴³ The resulting charge spillage, which estimates the error in the expansion, is only 0.2%, indicating the high quality of the basis orbitals.

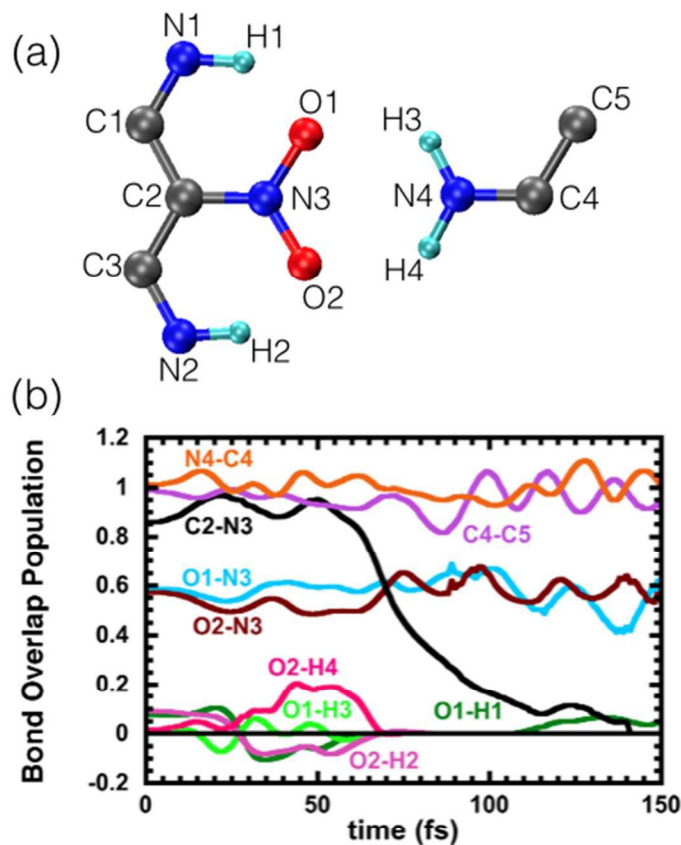


Fig. 5 Chemical bond dynamics. (a) Key atoms involved in one of the NO_2 dissociation reactions in the α -axis collision. (b) Bond overlap population between key atomic pairs involved in the reaction.

Figure 5(a) shows key atoms involved in one of the NO_2 dissociation reactions, while Fig. 5(b) shows the time evolution of the BOP between them. Figure 5(b) shows a gradual breakage of a CN bond (labelled C2-N3) around 70-140 fs. Formation of a strong inter-molecular hydrogen bond (*i.e.*, O2-H4 around 30-70 fs) indeed precedes the C-N scission as discussed above. Despite the loss of BOP between C2 and N3, no other pair shows a clear increase of BOP to compensate it. This reflects a rather delocalized transfer of electrons across many atoms.

It should be noted here that the transient HOMO-LUMO gap closing observed near the collision front in our simulation is distinct from bulk metallization under homogeneous deformation at much longer space and time scales. Under homogeneous compression, both experiments⁴⁴ and DFT calculations⁴⁵ show the absence of bulk metallization below a pressure of 100 GPa. The transient, heterogeneous gap closing found in our simulation occurs within 10^{-13} s after the collision or within 10^{-9} m from the collision front. This is exactly the athermal mechanochemical spatiotemporal regime expected for the inverse Jahn-Teller effect.^{1, 10} Subsequently, the energy gap should reopen as the molecular fragments relax to their local minimum-energy configurations.

In order to understand anisotropic reactions initiated at such hot spots, we have performed another six sets of simulations at a higher collision speed of 20 km/s, which is above the detonation speed of TATB crystals. Figure 6 shows the comparison of the number of fragments, temperature and Kohn-Sham eigenenergies for the α - and c -axis collisions.³⁹ Figures 6(a) and 6(b) show that most the fragments of α - and c -axis collisions (three

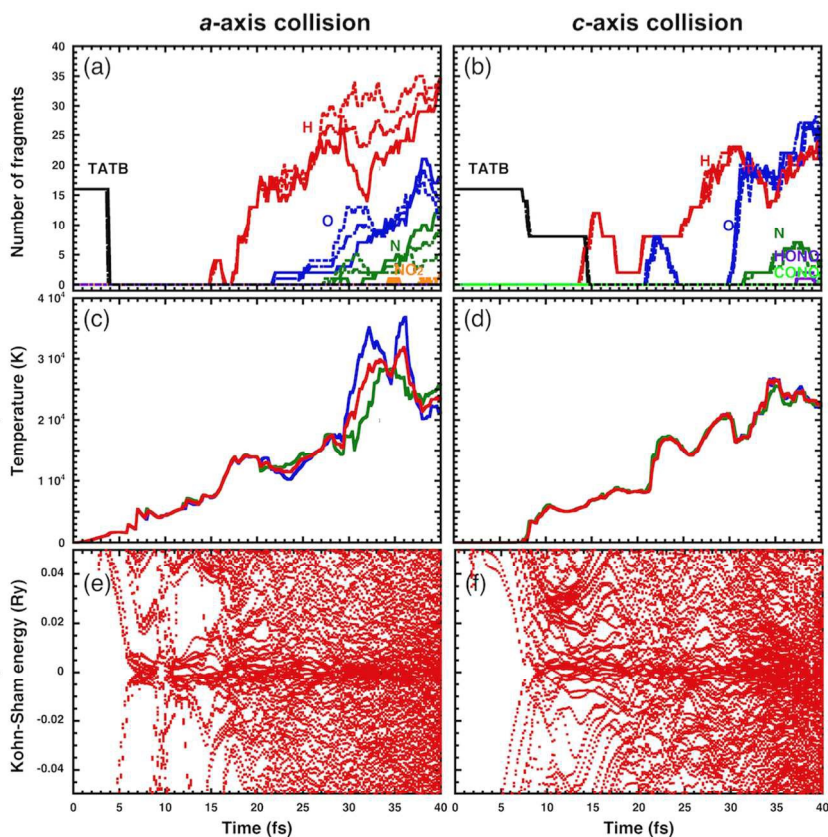


Fig. 6 Time evolution of the *a*- and *c*-axis collision simulations with a speed of 20 km/s. (a) and (b) show the number of molecular fragments, (c) and (d) show the temperature, and (e) and (f) show the Kohn-Sham eigenenergies. The left and right columns are for the *a*-axis and *c*-axis collisions, respectively, each with three different trajectories. Also see Fig. S2 for details of Kohn-Sham eigenenergies for the additional trajectories.

trajectories each collision) during the collision at 20 km/s are atomized atoms, such as H, O and N. In addition, some NO₂ fragments are found at the end of the *a*-axis collision. On the other hand, HONO and CONO molecules are observed in the *c*-axis collision. The temperature in Figs. 6(c) and 6(d) show that the *a*-axis collision produces more heat than the *c*-

axis collision. The very rapid closing of the HOMO-LUMO gap in both *a*- and *c*-axis collisions are shown in Figs. 6(e) and 6(f) (Four more trajectories also show similar look of the Kohn-Sham eigenenergies as a function of time for 20 km/s *a*- and *c*-axis collisions, see details in Fig. S2(a), S2(b), S2(c) and S2(d) , in Electronic Supplementary Information). Overall, crystalline anisotropy very similar to 6 km/s collision persists up to much higher velocities.

Conclusions

The atomistic understanding obtained by our nanocollider may pave a way toward rational design for insensitive energetic nanomaterials⁴⁶ and detonation synthesis of novel nanomaterials, such as nanodiamond.⁴⁷ Our QMD simulations identify specific events and their molecular origin that initiate chemical reactions under shock. Specifically, the present

simulations suggest the avoidance of localized load-bearing motifs (*e.g.*, a small number of interlayer N-N contacts) for designing more insensitive energetic materials. QMD simulations dynamically follow reaction pathways and are thereby able to predict unique reaction products.

Acknowledgements

This work was supported by the Office of Naval Research Grant No. N000014-12-1-0555. Simulations were performed at the Center for High-Performance Computing of the University of Southern California.

Reference

1. J. J. Gilman, *Science*, 1996, **274**, 65-65.
2. D. A. Davis, A. Hamilton, J. L. Yang, L. D. Cremar, D. Van Gough, S. L. Potisek, M. T. Ong, P. V. Braun, T. J. Martinez, S. R. White, J. S. Moore and N. R. Sottos, *Nature*, 2009, **459**, 68-72.
3. J. N. Brantley, K. M. Wiggins and C. W. Bielawski, *Science*, 2011, **333**, 1606-1609.
4. B. A. Beiermann, S. L. B. Kramer, J. S. Moore, S. R. White and N. R. Sottos, *ACS Macro Lett*, 2012, **1**, 163-166.
5. L. P. Wang, A. Titov, R. McGibbon, F. Liu, V. S. Pande and T. J. Martinez, *Nat Chem*, 2014, **6**, 1044-1048.
6. J. H. Lee, P. E. Loya, J. Lou and E. L. Thomas, *Science*, 2014, **346**, 1092-1096.
7. C. R. Hickenboth, J. S. Moore, S. R. White, N. R. Sottos, J. Baudry and S. R. Wilson, *Nature*, 2007, **446**, 423-427.
8. D. W. Brenner, D. H. Robertson, M. L. Elert and C. T. White, *Phys Rev Lett*, 1993, **70**, 2174-2177.
9. E. J. Reed, M. R. Manaa, L. E. Fried, K. R. Glaesemann and J. D. Joannopoulos, *Nat Phys*, 2008, **4**, 72-76.
10. J. J. Gilman, *Mater Sci Tech-Lond*, 2006, **22**, 430-437.
11. M. R. Manaa, *Appl Phys Lett*, 2003, **83**, 1352-1354.
12. V. M. Boddu, D. S. Viswanath, T. K. Ghosh and R. Damavarapu, *J Hazard Mater*, 2010, **181**, 1-8.
13. Z. F. Wang, Q. X. Li, H. B. Su, X. P. Wang, Q. W. Shi, J. Chen, J. L. Yang and J. G. Hou, *Phys Rev B*, 2007, **75**.
14. D. Le, A. Kara, E. Schroder, P. Hyldgaard and T. S. Rahman, *J Phys-Condens Mat*, 2012, **24**.
15. L. M. Liu, R. Car, A. Selloni, D. M. Dabbs, I. A. Aksay and R. A. Yetter, *J Am Chem Soc*, 2012, **134**, 19011-19016.
16. B. B. Averkiev, Z. A. Dreger and S. Chaudhuri, *J Phys Chem A*, 2014, **118**, 10002-10010.

17. B. Hunt, J. D. Sanchez-Yamagishi, A. F. Young, M. Yankowitz, B. J. LeRoy, K. Watanabe, T. Taniguchi, P. Moon, M. Koshino, P. Jarillo-Herrero and R. C. Ashoori, *Science*, 2013, **340**, 1427-1430.
18. A. K. Geim and I. V. Grigorieva, *Nature*, 2013, **499**, 419-425.
19. C. J. Wu, F. H. Ree and C. S. Yoo, *Propell Explos Pyrot*, 2004, **29**, 296-303.
20. A. C. Landerville, I. I. Oleynik and C. T. White, *J Phys Chem A*, 2009, **113**, 12094-12104.
21. F. Shimojo, S. Ohmura, R. K. Kalia, A. Nakano and P. Vashishta, *Phys Rev Lett*, 2010, **104**.
22. K. Shimamura, F. Shimojo, R. K. Kalia, A. Nakano and P. Vashishta, *Phys Rev Lett*, 2013, **111**.
23. K. Shimamura, F. Shimojo, R. K. Kalia, A. Nakano, K. Nomura and P. Vashishta, *Nano Lett*, 2014, **14**, 4090-4096.
24. N. A. Romero, A. Nakano, K. M. Riley, F. Shimojo, R. K. Kalia, P. Vashishta and P. C. Messina, *Computer*, 2015, **48**, 33-41.
25. P. Hohenberg and W. Kohn, *Physical Review*, 1964, **136**, B864-B871.
26. L. Z. Zhang, S. V. Zybin, A. C. T. van Duin, S. Dasgupta, W. A. Goddard and E. M. Kober, *J Phys Chem A*, 2009, **113**, 10619-10640.
27. M. R. Manaa, E. J. Reed, L. E. Fried and N. Goldman, *J Am Chem Soc*, 2009, **131**, 5483-5487.
28. D. E. Taylor, *J Phys Chem A*, 2013, **117**, 3507-3520.
29. R. H. Gee, S. Roszak, K. Balasubramanian and L. E. Fried, *J Chem Phys*, 2004, **120**, 7059-7066.
30. T. Tran, C. Tarver, J. Maienschein, P. Lewis, M. Moss, R. Druce, R. Lee and F. Roeske, *12th International Detonation Symposium Proceedings*, 2002.
31. P. E. Blochl, *Phys Rev B*, 1994, **50**, 17953-17979.
32. J. P. Perdew, K. Burke and M. Ernzerhof, *Phys Rev Lett*, 1996, **77**, 3865-3868.
33. S. Grimme, *J Comput Chem*, 2006, **27**, 1787-1799.
34. S. G. Louie, S. Froyen and M. L. Cohen, *Phys Rev B*, 1982, **26**, 1738-1742.
35. F. Shimojo, S. Hattori, R. K. Kalia, M. Kunaseth, W. W. Mou, A. Nakano, K. Nomura, S. Ohmura, P. Rajak, K. Shimamura and P. Vashishta, *J Chem Phys*, 2014, **140**.
36. K. I. Nomura, R. K. Kalia, A. Nakano, P. Vashishta, A. C. T. van Duin and W. A. Goddard, *Phys Rev Lett*, 2007, **99**.
37. A. Strachan, A. C. T. van Duin, D. Chakraborty, S. Dasgupta and W. A. Goddard, *Phys Rev Lett*, 2003, **91**.
38. Y. Li, R. K. Kalia, A. Nakano, K. I. Nomura and P. Vashishta, *Appl Phys Lett*, 2014, **105**.
39. D. D. Dlott, in *Overviews of Recent Research on Energetic Materials*, eds. R. W. Shaw, T. B. Brill and D. L. Thompson, World Scientific, Singapore, 2005, vol. 16, pp. 303-333.
40. R. S. Mulliken, *The Journal of Chemical Physics*, 1955, **23**, 1833-1840.
41. M. D. Segall, R. Shah, C. J. Pickard and M. C. Payne, *Phys Rev B*, 1996, **54**, 16317-16320.
42. O. F. Sankey and D. J. Niklewski, *Phys Rev B*, 1989, **40**, 3979-3995.
43. J. M. Soler, E. Artacho, J. D. Gale, A. Garcia, J. Junquera, P. Ordejon and D. Sanchez-Portal, *J Phys-Condens Mat*, 2002, **14**, 2745-2779.
44. A. J. Davidson, R. P. Dias, D. M. Dattelbaum and C. S. Yoo, *J Chem Phys*, 2011, **135**.
45. C. J. Wu, L. H. Yang, L. E. Fried, J. Quenneville and T. J. Martinez, *Phys Rev B*, 2003, **67**.
46. Z. Wang, X. Guo, F. Wu and T. Yan, *Propell Explos Pyrot*, 2015, DOI: 10.1002/prep.201500136.
47. V. Pichot, B. Risse, F. Schnell, J. Mory and D. Spitzer, *Sci Rep-Uk*, 2013, **3**.

